

# Mixed-Potential Volume Integral-Equation Approach for Circular Spiral Inductors

Behzad Rejaei

**Abstract**—The electromagnetic behavior of circular spiral inductors on layered substrates is analyzed by using the concentric ring approximation. The problem is formulated in terms of mixed-potential volume integral equations. The latter are semianalytically solved within the quasi-one-dimensional approximation. The result is a fast computationally efficient model, which takes into account substrate RF loss, as well as nonuniform current density distribution across inductor windings. The results are in good agreement with experimental data from various inductors on both low- and high-resistivity silicon substrates.

**Index Terms**—Eddy currents, mixed-potential integral-equation (MPIE) method, monolithic inductors, spiral inductors, substrate RF loss.

## I. INTRODUCTION

THE DEMAND for full integration of RF transceiver systems has been the driving force behind the recent surge of interest in on-chip inductors and—to a lesser extent—transformers. Emphasis lies on integration in silicon (Si) technology, which offers the most in terms of reliability, low cost, and a high level of integration. The major drawback of Si-based devices is, however, their proneness to significant RF losses caused by the current flow in the conductive substrate.

Although the inductance of lumped elements can be predicted with reasonable accuracy [1]–[6], the analysis of substrate RF losses is not straightforward. The common strategy is, therefore, based on empirical or semiempirical lumped-element representations [7]–[11], where substrate effects are modeled by using lumped capacitors and resistors, determined through comparison with experimental data. Despite its inherent simplicity, this method lacks the predictive power required for component design and optimization.

An alternative approach is to use comprehensive computational techniques [12]–[19] or semianalytical methods [20], [21]. In [12], inductor substrate losses were treated using a full-wave electromagnetic (EM) numerical package. The spectral-domain method of moments (MOM) was exploited in [13] to analyze spiral inductors on multilayered Si substrates. Reference [17] presented an analysis of planar [two-dimensional (2-D)] devices based on the mixed-potential

integral-equation (MPIE) method, generalized to three-dimensional (3-D) conductors in [18]. Reference [19] used the MOM and the finite-difference time-domain technique to analyze the nonuniform current distribution in inductor windings. The work of [20] was based on a volume integral-equation approach, but used the Greenhouse algorithm [2] to evaluate the partial inductances. In [21], this method was generalized to include substrate eddy currents, which are significant in highly doped low-resistivity substrates.

In spite of their power and generality, these numerical techniques usually do not offer the high computational speeds required for inductor optimization in mixed-level circuit/component design. This is because they require the division of the conductor volume (or surface) into a relatively large number of segments, and numerical evaluation of the corresponding Green's matrix elements on arbitrary substrates. Significant reduction of computation time could be achieved if the field equations were to be analytically solved in one direction (e.g., along the windings), effectively reducing the dimensionality of the problem. Such a model was previously presented by Rejaei *et al.* [22] by using the concentric-ring approximation of circular spiral inductors [3]. Here, a planar circular spiral inductor is replaced by a series connection of concentric rings, and the resulting rotational symmetry is exploited to semianalytically solve the field equations within the MPIE formalism. It should be mentioned that expressions for the inductance and quality factor of a single ring above a layered (magnetic) substrate were already derived in [23], but did not account for losses due to capacitive coil-substrate coupling.

In this paper, we present the full mathematical framework of the method of [22] and extend the latter to 3-D conductors, including the effect of the nonuniform current distribution (skin effect, current crowding) in the coil windings. Employing the MPIE technique, a solution is obtained by using a discrete Fourier transform along the rings, followed by application of Galerkin's method to compute the field distribution across each ring. The result is a fast predictive model for circular spiral inductors on layered substrates. The model is derived in Section II and compared to measurement data in Section III.

## II. CONCENTRIC-RING MODEL

The concentric-ring model of circular spiral inductors [3] results from replacing an  $N$ -turn spiral by a series connection of  $N$  circular rings (Fig. 1). It is assumed that the width  $w$  and spacing  $s$  of the rings are identical to those of the spiral inductor. The overall dimension of the concentric-ring model is

Manuscript received November 20, 2003; revised February 19, 2004.

The author is with the Faculty of Electrical Engineering, Mathematics, and Computer Science, Laboratory of Electronic Components, Technology, and Materials, Delft Institute of Microelectronics and Submicron Technology, Delft University of Technology, 2628 CT Delft, The Netherlands (e-mail: b.rejaei@ewi.tudelft.nl).

Digital Object Identifier 10.1109/TMTT.2004.831567

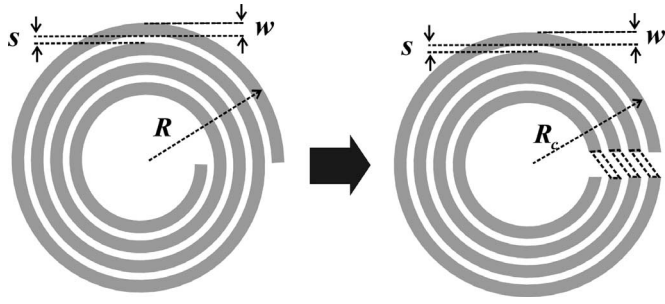


Fig. 1. Concentric-ring model of a circular spiral inductor. The width  $w$  and spacing  $s$  of the rings equal those of the inductor. The radius  $R_c$  is determined by requiring the outermost ring to have the same length as the first winding of the spiral inductor.

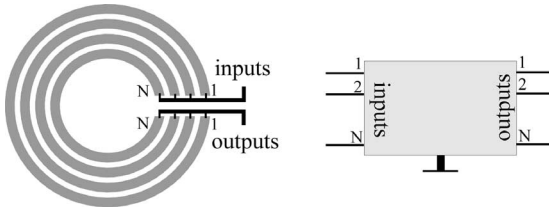


Fig. 2. System of concentric rings as a  $2N$ -port system.

determined by equating the total lengths of the inductors (at the midline).<sup>1</sup>

To fully exploit the rotational symmetry of the model, we next assume that the rings are disconnected. The set of concentric rings can then be viewed as a  $2N$ -port system with  $N$  inputs and outputs (Fig. 2). Once the admittance matrix (or, equivalently, the impedance matrix) of the  $2N$ -port system is calculated, the admittance matrix of the spiral inductor is retrieved by connecting the rings again. Note that, since the calculation of the admittance matrix of the system of rings is independent of the way the terminals are interconnected, this method can be easily generalized to investigate various structures such as transformers and stacked inductors built on several metal layers over layered substrates. In the remainder of this section, we will present the derivation of the model in detail in several steps.

### A. MPIEs

The starting point of our analysis is the MPIE approach [14]–[18]. Consider a multiply connected conductor consisting of  $N$  concentric rings with the volumes  $V_i$ ,  $i = 1, 2, \dots, N$ , placed on a substrate consisting of infinitely extended planar layers parallel to the  $x$ - $y$ -plane (Fig. 3).

Neglecting the Lorentz force, the current density  $\mathbf{J}$  at each point inside the conductor is given by the Ohm's law

$$\rho \mathbf{J}(\mathbf{r}) = \mathbf{E}(\mathbf{r}) = -j\omega \mathbf{A}(\mathbf{r}) - \nabla \Phi(\mathbf{r}) \quad (1)$$

<sup>1</sup>Simulations carried out by using HP ADS/Momentum (not shown here) demonstrate that the concentric ring approximation is fairly accurate even if the shape of the inductor windings significantly deviates from that of an ideal ring, e.g., when  $s > w$ . The resulting error in inductance and quality factor was found to be less than 4% for typical on-chip inductors built on lossy substrates. Furthermore, many practical structures are not spirals, but symmetric inductors where the actual windings are indeed rings.

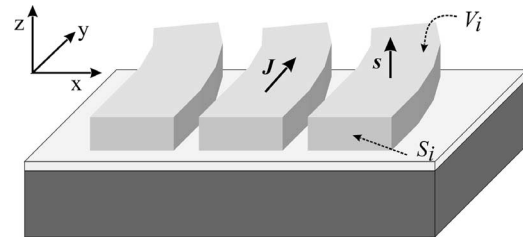


Fig. 3. Cross section of the system of rings. The volume and vertical cross section of the  $i$ th ring are denoted by  $V_i$  and  $S_i$ , respectively.  $\mathbf{s}$  is the unit normal to the conductor surface.

where  $\rho$  is the conductor resistivity,  $\mathbf{E}$  is the electric field, and  $\mathbf{A}$  and  $\Phi$  are the vector scalar potentials, respectively. The latter can be expressed as

$$\mathbf{A}(\mathbf{r}) = \int_V \overline{\mathbf{K}}(\mathbf{r}, \mathbf{r}') \cdot \mathbf{J}(\mathbf{r}') dV' \quad (2)$$

$$\Phi(\mathbf{r}) = \int_V G(\mathbf{r}, \mathbf{r}') n(\mathbf{r}') dV' \quad (3)$$

where  $V = \cup_{i=1}^N V_i$  is the total volume of the conductor,  $n$  denotes the charge density,  $\mathbf{r} = (x, y, z)$ ,  $\nabla = (\partial_x, \partial_y, \partial_z)$ , and  $dV' = dx' dy' dz'$ . The form of the  $3 \times 3$  matrix  $\overline{\mathbf{K}}$  and the scalar  $G$  Green's functions depend on the gauge chosen [16]. We choose for the representation in [14] where

$$\overline{\mathbf{K}}_{xx} = \overline{\mathbf{K}}_{yy} \equiv K \quad \overline{\mathbf{K}}_{xy} = \overline{\mathbf{K}}_{yx} = 0. \quad (4)$$

Note that, in (2) and (3), the dependence on the Green's functions on frequency  $\omega$  is not shown explicitly.

Using (1)–(3) and the continuity equation  $\nabla \cdot \mathbf{J} = -j\omega n$ , one arrives at the closed set of integro-differential equations

$$-\nabla \Phi(\mathbf{r}) = \rho \mathbf{J}(\mathbf{r}) + j\omega \int_V \overline{\mathbf{K}}(\mathbf{r}, \mathbf{r}') \cdot \mathbf{J}(\mathbf{r}') dV' \quad (5)$$

$$-\Phi(\mathbf{r}) = \frac{1}{j\omega} \int_V G(\mathbf{r}, \mathbf{r}') \nabla' \cdot \mathbf{J}(\mathbf{r}') dV'. \quad (6)$$

In order to allow a complete solution, (5) and (6) should be supplemented by boundary conditions for  $\Phi$  and/or the normal component of the current density  $J^s = \mathbf{J} \cdot \mathbf{s}$  on the surface of the conductor ( $\mathbf{s}$  is the unit vector normal to the surface). On the interfaces between external contacts and the conductor, either  $\Phi$  or  $J^s$  should be specified, whereas  $J^s$  should vanish everywhere else on the surface of the conductor.

In this paper, we shall restrict ourselves to substrates consisting of isotropic layers, i.e., where each layer is described by isotropic constitutive parameters. The resulting rotational symmetry of the system is then reflected in the relations

$$G(\mathbf{r}, \mathbf{r}') = G(R; z, z'), K(\mathbf{r}, \mathbf{r}') = K(R; z, z') \quad (7a)$$

$$R = [(x - x')^2 + (y - y')^2]^{\frac{1}{2}}. \quad (7b)$$

The spectral-domain representation of the Green's functions  $G$  and  $K$  is given in the Appendix.

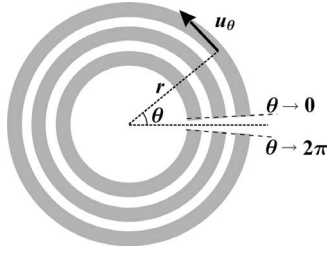


Fig. 4. Concentric-ring system in cylindrical coordinates.  $\mathbf{u}_\theta$  is the azimuthal unit vector. The input and output of the rings are denoted by the limits  $\theta \rightarrow 0$  and  $\theta \rightarrow 2\pi$ .

### B. Quasi-One-Dimensional (1-D) Approximation

Employing cylindrical coordinates  $(r, z, \theta)$ , we next adopt the quasi-1-D approximation by neglecting the components of  $\mathbf{J}$  and variations of  $\Phi$  in the radial ( $r$ )- and vertical ( $z$ )-directions inside the rings

$$\begin{cases} \mathbf{J}(\mathbf{r}) = J_i(r, z, \theta)\mathbf{u}_\theta(\mathbf{r}), \\ \Phi(\mathbf{r}) = \Phi_i(\theta) \end{cases}, \quad \text{for } \mathbf{r} \in V_i \quad (8)$$

where  $\mathbf{u}_\theta$  is the azimuthal unit vector (Fig. 4). Here, in fact, we have assumed that current follows the direction of the rings inside the conductor. Using (5)–(8), one then arrives at the integral equations

$$-\frac{\partial \Phi_i(\theta)}{r \partial \theta} = \rho J_i(r, z, \theta) + j\omega \sum_{k=1}^N \int_{V_k} K_c(R; z, z') J_k(r', z', \theta') dV' \quad (9)$$

$$-\Phi_i(\theta) = \frac{1}{j\omega} \sum_{k=1}^N \int_{V_k} G(R; z, z') \frac{\partial J_k(r', z', \theta')}{r' \partial \theta'} dV' \quad (10)$$

where  $dV' = r' dr' dz' d\theta'$  and

$$K_c(R; z, z') = K(R; z, z') \cos(\theta - \theta'). \quad (11)$$

In (9) and (10),  $G(R; z, z')$  and  $K_c(R; z, z')$  are periodic functions of  $\varphi = \theta - \theta'$  with the period  $2\pi$ . This is because  $R = [r^2 + r'^2 - 2rr' \cos \varphi]^{1/2}$  in cylindrical coordinates. One can, therefore, expand  $G$  and  $K_c$  in the Fourier series

$$G(R; z, z') = \frac{1}{2\pi} \sum_{n=-\infty}^{\infty} \mathcal{G}^n(r, z; r', z') e^{jn\varphi} \quad (12a)$$

$$K_c(R; z, z') = \frac{1}{2\pi} \sum_{n=-\infty}^{\infty} \mathcal{K}^n(r, z; r', z') e^{jn\varphi} \quad (12b)$$

$$\mathcal{G}^n(r, z; r', z') = \int_0^{2\pi} G(R; z, z') e^{-jn\varphi} d\varphi \quad (12c)$$

$$\mathcal{K}^n(r, z; r', z') = \int_0^{2\pi} K_c(R; z, z') e^{-jn\varphi} d\varphi. \quad (12d)$$

Note that  $\mathcal{G}^n = \mathcal{G}^{-n}$  and  $\mathcal{K}^n = \mathcal{K}^{-n}$  because  $G$  and  $K_c$  actually are even functions of  $\varphi$  due to reflection symmetry in the  $x$ - $y$ -plane.

Equations (12a)–(12d) can be used to transform (9) and (10) into a set of decoupled integral equations by applying the Fourier transformations

$$\mathcal{J}_i^m(r, z) = \frac{1}{2\pi} \int_0^{2\pi} J_i(r, z, \theta) e^{-jm\theta} d\theta \quad (13a)$$

$$\phi_i^m = \frac{1}{2\pi} \int_0^{2\pi} \Phi_i(\theta) e^{-jm\theta} d\theta \quad (13b)$$

$$J_i(r, z, \theta) = \sum_{m=-\infty}^{\infty} \mathcal{J}_i^m(r, z) e^{jm\theta} \quad (13c)$$

$$\Phi_i(\theta) = \sum_{m=-\infty}^{\infty} \phi_i^m e^{jm\theta}. \quad (13d)$$

After multiplying (9) and (10) by  $e^{-jm\theta}$ , calculating the integral over  $\theta$  from 0 to  $2\pi$ , and using (13a) and (13b), one arrives at

$$\Delta \Phi_i - jm \phi_i^m = \rho r \mathcal{J}_i^m(r, z) + j\omega \sum_{k=1}^N \int_{S_k} \mathcal{K}^m(r, z; r', z') \times \mathcal{J}_k^m(r', z') r r' dS' \quad (14)$$

$$\phi_i^m = \frac{1}{j\omega} \sum_{k=1}^N \int_{S_k} \mathcal{G}^m(r, z; r', z') \eta_k^m(r', z') dS'. \quad (15)$$

Here, the integrations are carried out over the cross sections  $S_k$  of the rings in the  $r$ - $z$ -plane (perpendicular to the azimuthal unit vector  $\mathbf{u}_\theta$ ),  $dS' = dr' dz'$ , and

$$\eta_k^m(r, z) = \Delta J_k(r, z) - jm \mathcal{J}_k^m(r, z) \quad (16a)$$

$$\Delta \Phi_i = \frac{1}{2\pi} (\Phi_i^{\text{in}} - \Phi_i^{\text{out}}) \quad (16b)$$

$$\Delta J_i(r, z) = \frac{1}{2\pi} [J_i^{\text{in}}(r, z) - J_i^{\text{out}}(r, z)] \quad (16c)$$

$$\Phi_i^{\text{in}} = \lim_{\theta \rightarrow 0} \Phi_i(\theta) \quad (16d)$$

$$J_i^{\text{in}}(r, z) = \lim_{\theta \rightarrow 0} J_i(r, z, \theta) \quad (16d)$$

$$\Phi_i^{\text{out}} = \lim_{\theta \rightarrow 2\pi} \Phi_i(\theta) \quad (16e)$$

$$J_i^{\text{out}}(r, z) = \lim_{\theta \rightarrow 2\pi} J_i(r, z, \theta) \quad (16e)$$

where  $\Phi_i^{\text{in}}$ ,  $J_i^{\text{in}}(r, z)$  and  $\Phi_i^{\text{out}}$ ,  $J_i^{\text{out}}(r, z)$  denote the potential and current density on the input ( $\theta \rightarrow 0$ ) and output ( $\theta \rightarrow 2\pi$ ) cross sections of the  $i$ th ring, respectively (Fig. 4). Note that  $\phi_i^m$  and  $\Delta \Phi_i$  are constant on  $S_i$ , but depend on the ring index  $i$ .

### C. Solution of the Integral Equations

For each harmonic mode  $m$ , (14) is a Fredholm integral equation of the second kind for the functions  $\mathcal{J}_i^m(r, z)$ , whereas (15) is a Fredholm integral equation of the first kind for the functions  $\eta_i^m(r, z)$ . Both equations can be numerically solved by Galerkin's method, where one approximates  $\mathcal{J}_i^m(r, z)$  and  $\eta_i^m(r, z)$  by an expansion in terms of a finite number ( $M_i$ )

of basis functions  $f_{i\alpha}(r, z)$ , respectively,  $g_{i\alpha}(r, z)$  on  $S_i$  as follows:

$$\mathcal{J}_i^m(r, z) \approx \sum_{\alpha=1}^{M_i} u_{i\alpha}^m f_{i\alpha}(r, z) \quad (17a)$$

$$\eta_i^m(r, z) \approx \sum_{\alpha=1}^{M_i} w_{i\alpha}^m g_{i\alpha}(r, z). \quad (17b)$$

Multiplication of both sides of (14) and (15) by the basis functions  $f_{i\alpha}$ , respectively,  $g_{i\alpha}$ , and integration over the ring cross sections results in matrix equations for the constants  $u_{i\alpha}^m$  and  $w_{i\alpha}^m$  with the solution

$$u_{i\alpha}^m = \sum_{k=1}^N \sum_{\beta=1}^{M_k} (\check{\mathcal{Q}} + j\omega\check{\mathcal{K}}^m)^{-1}_{i\alpha, k\beta} \nu_{k\beta} (\Delta\Phi_k - jm\phi_k^m) \quad (18)$$

$$w_{i\alpha}^m = \sum_{k=1}^N \sum_{\beta=1}^{M_k} j\omega(\check{\mathcal{G}}^m)^{-1}_{i\alpha, k\beta} \tau_{k\beta} \phi_k^m \quad (19)$$

where

$$\check{\mathcal{Q}}_{i\alpha, k\beta} = \rho\delta_{ik} \int_{S_i} f_{i\alpha}(r, z) f_{i\beta}(r, z) r dS \quad (20a)$$

$$\check{\mathcal{K}}_{i\alpha, k\beta}^m = \int_{S_i} \int_{S_k} f_{i\alpha}(r, z) \mathcal{K}^m(r, z; r', z') f_{k\beta}(r', z') r r' dS dS' \quad (20b)$$

$$\check{\mathcal{G}}_{i\alpha, k\beta}^m = \int_{S_i} \int_{S_k} g_{i\alpha}(r, z) \mathcal{G}^m(r, z; r', z') g_{k\beta}(r', z') dS dS' \quad (20c)$$

$$\nu_{i\alpha} = \int_{S_i} f_{i\alpha}(r, z) dS,$$

$$\tau_{i\alpha} = \int_{S_i} g_{i\alpha}(r, z) dS \quad (20d)$$

with  $\delta_{ik}$  denoting the Kronecker delta.

In order to reduce the computation time for the integrations in (20b) and (20c), we divide the cross section of the rings in rectangular segments and use the basis functions

$$f_{i\alpha}(r, z) = \begin{cases} r^{-1}, & \text{if } (r, z) \in S_{i\alpha} \\ 0, & \text{otherwise} \end{cases} \quad (21)$$

$$g_{i\alpha}(r, z) = \begin{cases} 1, & \text{if } (r, z) \in S_{i\alpha} \\ 0, & \text{otherwise} \end{cases}$$

where  $\alpha = 1, 2, \dots, M_i$  and  $S_{i\alpha}$  denotes the surface of the  $\alpha$ th rectangular segment on the cross section of the  $i$ th ring (Fig. 5). In the Appendix, we show that each element of the matrices  $\check{\mathcal{K}}_{i\alpha, k\beta}^m$  and  $\check{\mathcal{G}}_{i\alpha, k\beta}^m$  can then be calculated by performing a single integration in the spectral domain.

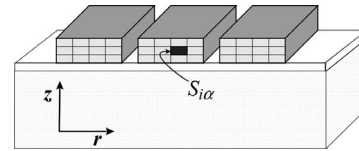


Fig. 5. Vertical cross section of each ring (in the  $r$ - $z$ -plane) is divided into rectangular segments.

#### D. Admittance Matrix of the System of Rings

In order to calculate the admittance matrix of the concentric-ring system, one has to find the relationship between the ring potentials  $\Phi_i(\theta)$  and the ring currents

$$I_i(\theta) = \int_{S_i} J_i(r, z, \theta) dS, \quad i = 1, 2, \dots, N \quad (22)$$

at the  $N$  inputs ( $\theta \rightarrow 0$ ) and outputs ( $\theta \rightarrow 2\pi$ ). Substitution of the Fourier series expansion (13c) in the above equation results in

$$I_i(\theta) = \sum_{m=-\infty}^{\infty} \mathcal{I}_i^m e^{jm\theta} \quad (23a)$$

$$\mathcal{I}_i^m = \int_{S_i} \mathcal{J}_i^m(r, z) dS \quad (23b)$$

where  $\mathcal{I}_i^m$  are the Fourier components of  $I_i$ . By integrating (17a) and (17b) over  $S_i$ , and using (16a)–(16e), (18), (19), (20d), and (22)–(23b), one obtains the matrix equations

$$\sum_{k=1}^N \check{\mathcal{Z}}_{ik}^m \mathcal{I}_k^m + 2\pi jm\phi_i^m = \Phi_i^{\text{in}} - \Phi_i^{\text{out}} \quad (24)$$

$$\sum_{k=1}^N \check{\mathcal{Y}}_{ik}^m \phi_k^m + 2\pi jm\mathcal{I}_i^m = I_i^{\text{in}} + I_i^{\text{out}} \quad (25)$$

in which

$$(\check{\mathcal{Z}}^m)_{ik}^{-1} = \frac{1}{2\pi} \sum_{\alpha=1}^{M_i} \sum_{\beta=1}^{M_k} (\check{\mathcal{Q}} + j\omega\check{\mathcal{K}}^m)^{-1}_{i\alpha, k\beta} \nu_{i\alpha} \nu_{k\beta} \quad (26a)$$

$$\check{\mathcal{Y}}_{ik}^m = 2\pi j\omega \sum_{\alpha=1}^{M_i} \sum_{\beta=1}^{M_k} (\check{\mathcal{G}}^m)^{-1}_{i\alpha, k\beta} \tau_{i\alpha} \tau_{k\beta} \quad (26b)$$

are  $N \times N$  matrices, and

$$I_i^{\text{in}} = \lim_{\theta \rightarrow 0} I_i(\theta) \quad I_i^{\text{out}} = - \lim_{\theta \rightarrow 2\pi} I_i(\theta) \quad (27)$$

designate the total current at the input, respectively, and output of the  $i$ th ring. (The minus sign has been included according to the conventional definition of port currents in network theory.) From (24) and (25), one can determine the Fourier coefficients  $\mathcal{I}_i^m$  and  $\phi_i^m$  in terms of  $\Phi_i^{\text{in}} - \Phi_i^{\text{out}}$  and  $I_i^{\text{in}} + I_i^{\text{out}}$ . After substituting the solution obtained (not shown here) in the Fourier series (13d) and (23b), evaluating  $I_i(\theta)$  and  $\Phi_i(\theta)$  in the limits

$\theta \rightarrow 0$  and  $\theta \rightarrow 2\pi$ , and applying several matrix manipulations, we arrive at the  $2N \times 2N$  admittance matrix  $\check{Y}$  as follows:

$$\check{Y} = \begin{bmatrix} \frac{1}{4}(\check{B})^{-1} + \check{A} & \frac{1}{4}(\check{B})^{-1} - \check{A} \\ \frac{1}{4}(\check{B})^{-1} - \check{A} & \frac{1}{4}(\check{B})^{-1} + \check{A} \end{bmatrix} \quad (28a)$$

$$\check{A} = \sum_{m=0}^{\infty} a_m \check{A}^m \quad (28b)$$

$$(\check{A}^m)^{-1} = \check{Z}^m + 4\pi^2 m^2 (\check{Y}^m)^{-1} \quad (28c)$$

$$(\check{B}^m)^{-1} = \check{Y}^m + 4\pi^2 m^2 (\check{Z}^m)^{-1} \quad (28d)$$

where  $a_0 = 1$  and  $a_{m>0} = 2$ . Note that the summation in (28b) only involves nonnegative  $m$ 's. This is because, as mentioned previously,  $\mathcal{G}^m = \mathcal{G}^{-m}$  and  $\mathcal{K}^m = \mathcal{K}^{-m}$  which, in turn, implies that  $\check{Z}^m = \check{Z}^{-m}$  and  $\check{Y}^m = \check{Y}^{-m}$ . Equations (28a)–(28d) together with the definitions (26a) and (26b) express the admittance matrix of the concentric-ring system in terms of the matrix elements of the Green's functions  $\mathcal{K}^m$  and  $\mathcal{G}^m$ .

It is important to note that  $\check{Z}^m$  and  $\check{Y}^m$  have, in fact, been computed from the vector-potential Green's function  $K$  and the scalar potential Green's function  $G$ , respectively. It is, therefore, natural to link  $\check{Z}^m$  and  $\check{Y}^m$  to the inductance, respectively, capacitance matrix of the system in the  $m$ th mode by introducing the decompositions

$$\check{Z}_{ik}^m = \check{R}_{ik}^m + j\omega \check{L}_{ik}^m \quad \check{Y}_{ik}^m = \check{G}_{ik}^m + j\omega \check{C}_{ik}^m \quad (29)$$

in which  $\check{R}_{ik}^m$ ,  $\check{L}_{ik}^m$ ,  $\check{G}_{ik}^m$ , and  $\check{C}_{ik}^m$  are real frequency-dependent  $N \times N$  matrices (see Fig. 6). Here,  $\check{L}_{ik}^m$  can be interpreted as the inductance matrix of  $N$  mutually coupled inductors. Similarly,  $\check{C}_{ik}^m$  represents  $N$  mutually coupled capacitors. The matrix  $\check{R}_{ik}^m$  takes account of the dc loss in the conductor, as well as additional RF loss due to nonuniform distribution of current density on the cross section of the windings (skin effect, current crowding). However, it also includes losses due to substrate eddy currents induced by the RF magnetic field. The matrix  $\check{C}_{ik}^m$ , on the other hand, contains substrate RF losses caused by the flow of substrate currents induced by the potential difference between different points on the conductor and between the conductor and reference ground. The latter has implicitly been defined as a point at the infinity, where the Green's functions vanish.

In practice, only a small number of modes (small  $m$ 's) will suffice to provide an adequate solution of the problem. Higher modes (larger  $m$ 's) become important at very high frequencies where the effective wavelength becomes smaller than the length of rings. The number of modes included in the calculation depends on the required accuracy and should be determined from numerical experimentation.

### E. Retrieving the Admittance Matrix of the Inductor

After the admittance matrix of the concentric-ring system is computed, the rings can be connected in series to obtain the

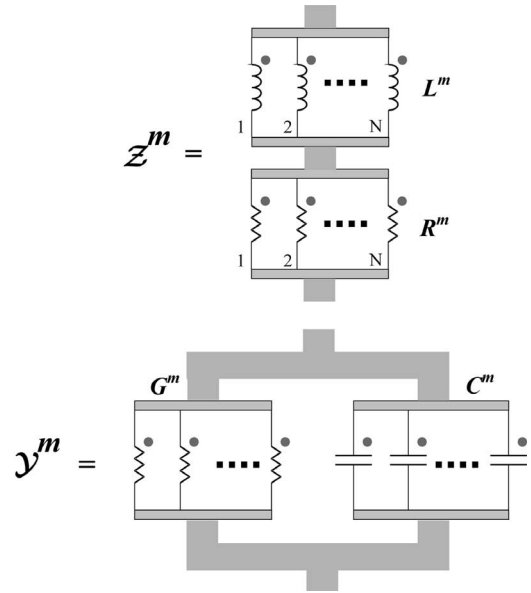


Fig. 6. Decomposition of the matrices  $\check{Z}^m$  and  $\check{Y}^m$  in terms of mutual resistance  $\check{R}^m$ , inductance  $\check{L}^m$ , conductance  $\check{G}^m$ , and capacitance  $\check{C}^m$  matrices for each mode  $m$ .

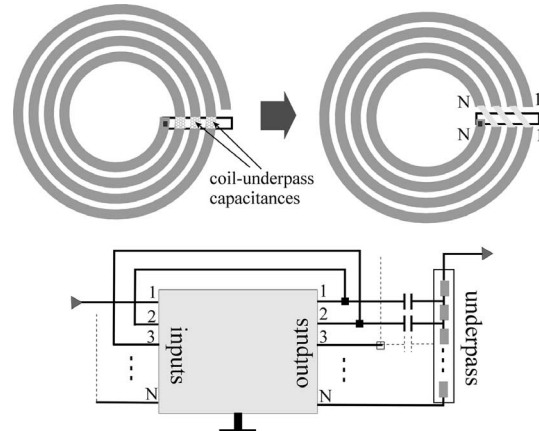


Fig. 7. Admittance matrix of the inductor is obtained by connecting the rings in series. The underpass is modeled as a stripline, capacitively interacting with the inductor windings through the  $N - 1$  metal-oxide-metal capacitors formed between the inductor and underpass metals.

TABLE I  
LAYER PARAMETERS FOR MEDIUM-RESISTIVITY (MR)  
AND LOW-RESISTIVITY (LR) Si SUBSTRATES

Substrate layer	Thickness ( $\mu\text{m}$ )	Dielectric constant	Conductivity (S/m)
Metal (Al)	1 (MR), 4 (LR)	-	$3.7 \times 10^7$
SiO <sub>2</sub>	4	3.9	0
Si	525	11.9	20 (MR), $10^4$ (LR)

$2 \times 2$  admittance matrix of the spiral inductor. In practical applications, however, an underpass is used to connect the inner terminal of the coil to other devices. It is not possible to directly include the underpass in the concentric-ring model due to the

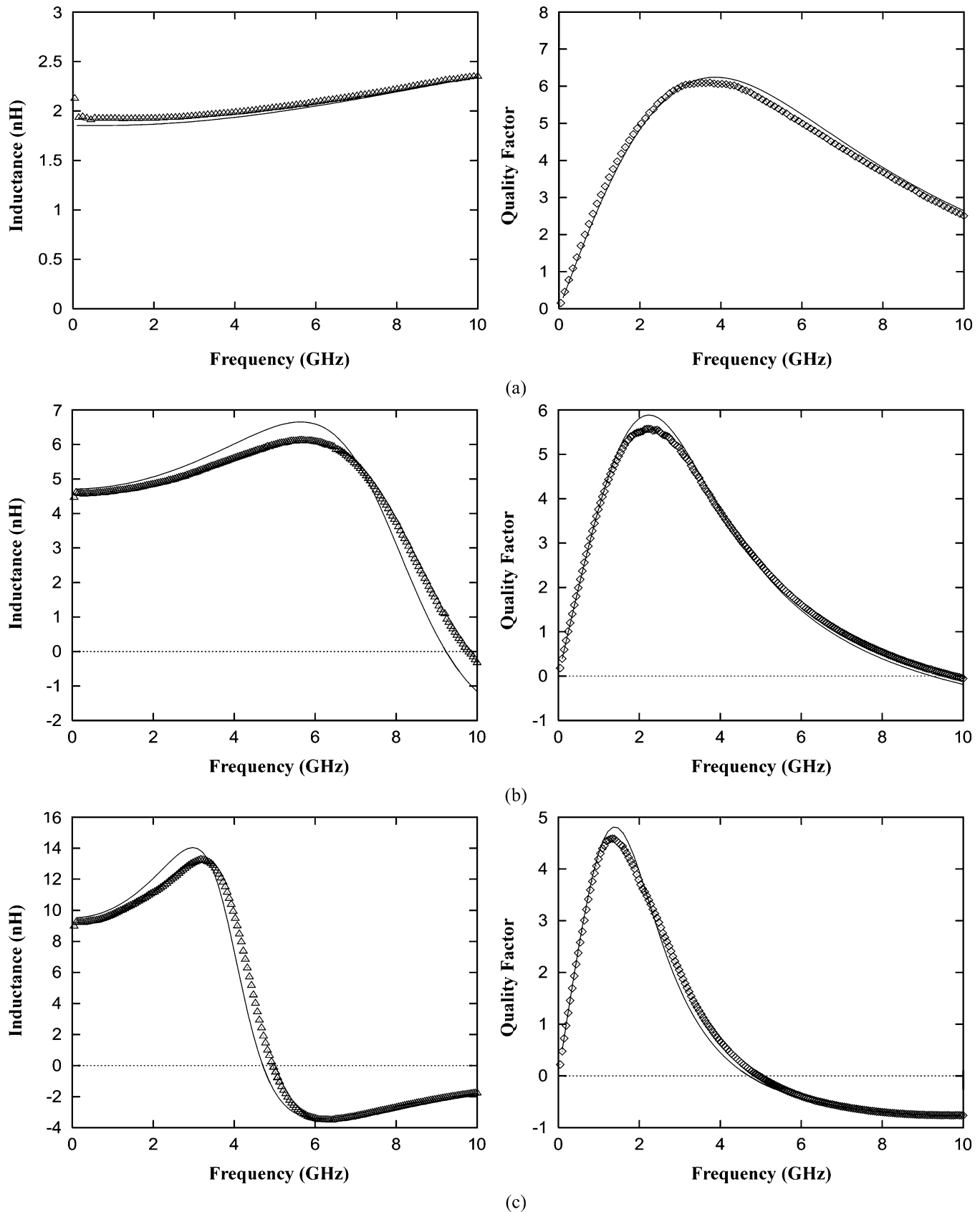


Fig. 8. Measured (markers) and simulated (solid lines) inductance and quality factor of circular spiral inductors. (a) Inductor A ( $N = 4, R = 120 \mu\text{m}, w = 13.7 \mu\text{m}, s = 10.27 \mu\text{m}$ ). (b) Inductor B ( $N = 4, R = 140 \mu\text{m}, w = 11.38 \mu\text{m}, s = 3 \mu\text{m}$ ). (c) Inductor C ( $N = 6, R = 160 \mu\text{m}, w = 11.25 \mu\text{m}, s = 3 \mu\text{m}$ ). Substrate resistivity was  $5 \Omega \cdot \text{cm}$ . Metal thickness was  $1 \mu\text{m}$ .

breaking of the circular symmetry. Nevertheless, in the special case of Fig. 7, one can approximately model the underpass

as a stripline interacting with the inductor through lumped metal–oxide–metal capacitors formed between the underpass

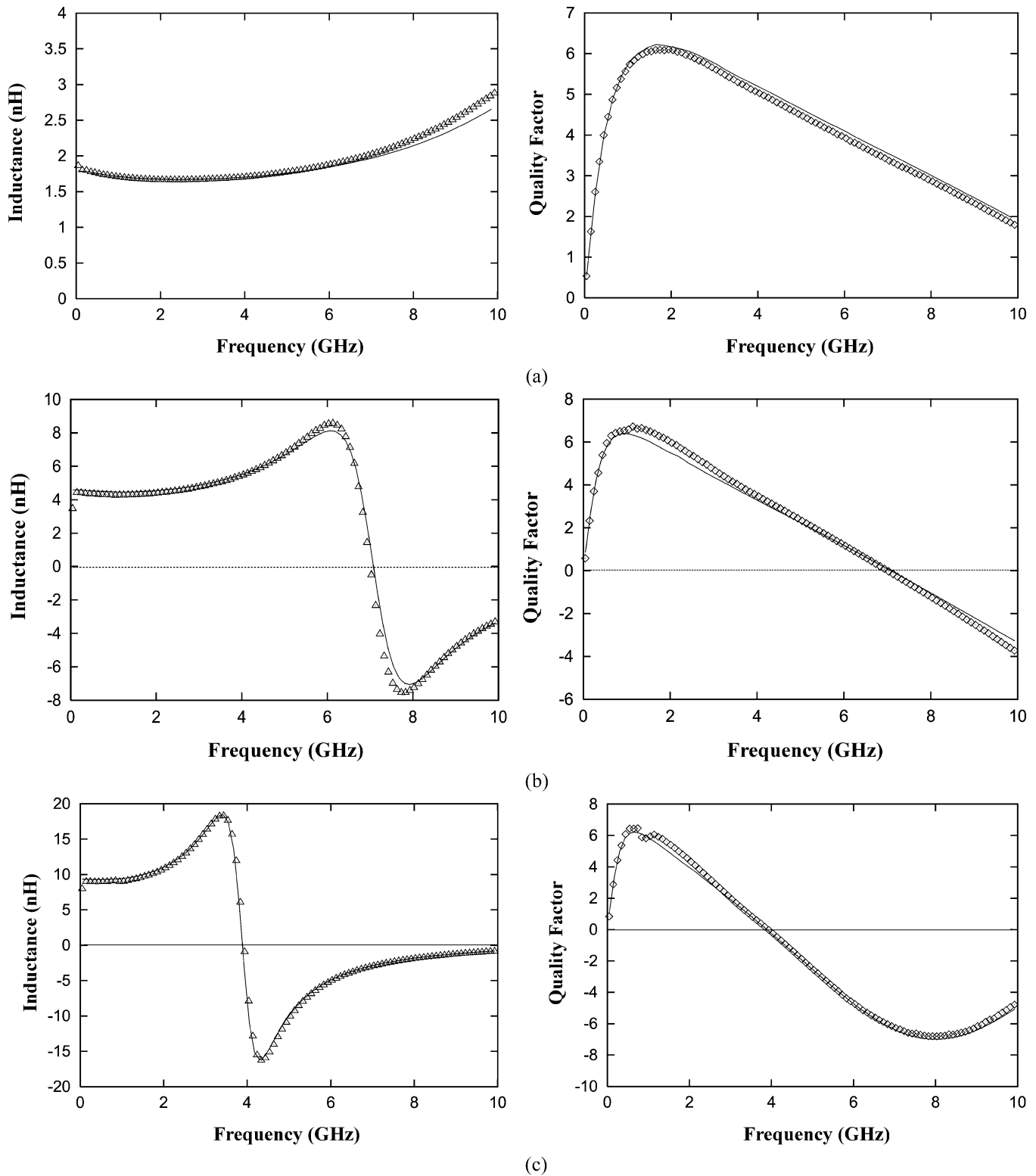


Fig. 9. Measured (markers) and simulated (solid lines) inductance and quality factor of circular spiral inductors. (a) Inductor A ( $N = 4$ ,  $R = 120 \mu\text{m}$ ,  $w = 13.7 \mu\text{m}$ ,  $s = 10.27 \mu\text{m}$ ). (b) Inductor B ( $N = 4$ ,  $R = 140 \mu\text{m}$ ,  $w = 11.38 \mu\text{m}$ ,  $s = 3 \mu\text{m}$ ). (c) Inductor C ( $N = 6$ ,  $R = 160 \mu\text{m}$ ,  $w = 11.25 \mu\text{m}$ ,  $s = 3 \mu\text{m}$ ). Substrate resistivity was  $0.01 \Omega \cdot \text{cm}$ . Metal thickness was  $4 \mu\text{m}$ .

and windings. Despite the neglect of the mutual inductance between the underpass and spiral coil, this approximation turns out to be accurate enough for typical integrated inductors, as shown by the experimental data in Section III.

### III. EXPERIMENTAL RESULTS

We have fabricated various spiral inductors on medium-resistivity ( $5 \Omega \cdot \text{cm}$ ) and low-resistivity ( $0.01 \Omega \cdot \text{cm}$ ) Si substrates.

TABLE II  
GEOMETRICAL PARAMETERS ( $N$ ,  $R$ ,  $w$ ,  $s$ ), INDUCTANCE AT MAXIMUM QUALITY FACTOR ( $L_{Q_{\max}}$ ), MAXIMUM QUALITY FACTOR ( $Q_{\max}$ ), AND SELF-RESONANCE FREQUENCY ( $f_{SR}$ ) OF THREE INDUCTORS ON MEDIUM- AND LOW-RESISTIVITY SUBSTRATES

Inductor	Geometrical Parameters				$5\Omega\text{-cm Si}$						$0.01\Omega\text{-cm Si}$					
	$N$	$R$ ( $\mu\text{m}$ )	$w$ ( $\mu\text{m}$ )	$s$ ( $\mu\text{m}$ )	$L_{Q_{\max}}$ (nH)		$Q_{\max}$		$f_{SR}$ (GHz)		$L_{Q_{\max}}$ (nH)		$Q_{\max}$		$f_{SR}$ (GHz)	
					meas.	sim.	meas.	sim.	meas.	sim.	meas.	sim.	meas.	sim.	meas.	sim.
A	4	120	13.7	10.27	1.99	1.93	6.11	6.26	19.98	19.62	1.67	1.68	6.09	6.22	12.77	13.03
B	4	140	11.38	3	4.96	5.17	5.59	5.90	9.77	9.26	4.28	4.47	6.71	6.41	6.98	7.07
C	6	160	11.25	3	10.20	10.69	4.56	4.83	4.94	4.71	9.05	9.29	6.46	6.22	3.91	3.88

Each substrate consists of a  $525\text{-}\mu\text{m}$ -thick Si layer, insulated by a  $4\text{-}\mu\text{m}$ -thick layer of  $\text{SiO}_2$ . The spiral coils were built by using the top metal layer (1- and  $4\text{-}\mu\text{m}$ -thick aluminum on 5- and  $0.01\text{-}\Omega\cdot\text{cm}$  substrates, respectively). The underpass contact was built by using an additional  $0.6\text{-}\mu\text{m}$ -thick metal layer, spaced  $0.8\text{ }\mu\text{m}$  below the top metal layer.

The  $S$ -parameter measurements were performed using an HP8510B/8514A network analyzer in combination with a Cascade Microtech Summit 9000 probe station with  $200\text{-}\mu\text{m}$ -pitch signal-ground probes. The calculated  $Y$ -parameters, after deembedding the measurement pads, are then used to calculate the inductance  $L$  and quality factor  $Q$  of each coil in the configuration where port 2 (connected to the inner terminal) is grounded as follows:<sup>2</sup>

$$L = \frac{1}{\omega} \text{Im}[Y_{11}] \quad Q = \frac{\text{Im}[Y_{11}]}{\text{Re}[Y_{11}]} \quad (30)$$

Table I lists the substrate parameters used in the simulations. The simulations were performed retaining the  $m = 0$  harmonic mode only since numerical experimentation revealed negligible improvement upon inclusion of higher modes. In order to take account of the nonuniform distribution of current and charge density, the cross section of each winding was divided into a number of rectangular segments (see Section II-C and the Appendix). The simulations were carried out on an HP Unix workstation. For a four-turn inductor, the computation time for each frequency point was less than  $0.22\text{ s}$  at five segments/winding and less than  $1.5\text{ s}$  at 25 segments/winding. The results shown below were obtained using 25 segments/winding.

Figs. 8 and 9 show the measured and simulated  $L$  and  $Q$  for three different inductors (A, B, and C), on the medium- and low-resistivity substrates. The geometrical parameters of the three coils, as well as their measured and simulated inductance at maximum quality factor ( $L_{Q_{\max}}$ ), maximum quality factor ( $Q_{\max}$ ), and self-resonance frequency ( $f_{SR}$ ) are listed in Table II. The discrepancy between the measured and simulated inductance curves for coils B and C in Fig. 8 can be attributed to the underestimation of their  $f_{SR}$  by the model on the  $5\text{-}\Omega\cdot\text{cm}$  substrate (Table II). However, one should note that the actual resistivity of the Si substrate may have differed from

<sup>2</sup>Unlike classical microwave substrates, Si technology does not allow the use of a through-wafer vias providing access to a backside metal layer (RF ground). In the experiments discussed here, large rectangular patches ( $800\text{ }\mu\text{m} \times 300\text{ }\mu\text{m}$ ) distanced  $300\text{ }\mu\text{m}$  away from the edge of the coils and built in the first metal layer were used as a ground pad for the probes. The large area of each patch provides a low-impedance path through the conductive substrate to the metallic chuck on which the wafers are placed during the measurement. The chuck replaces the backside metal as the RF ground.

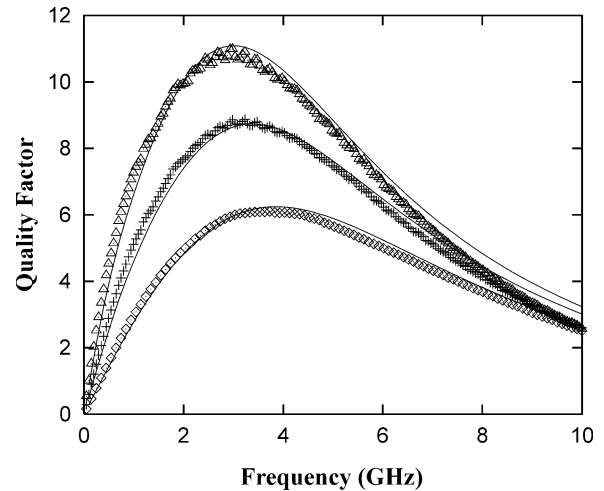


Fig. 10. Measured (markers) and simulated (solid lines) quality factor of inductor A ( $N = 4$ ,  $R = 120\text{ }\mu\text{m}$ ,  $w = 13.7\text{ }\mu\text{m}$ ,  $s = 10.27\text{ }\mu\text{m}$ ) built on the  $5\text{-}\Omega\cdot\text{cm}$  Si substrate using a 1-, 2-, and  $4\text{-}\mu\text{m}$ -thick Al layer.

the nominal value used ( $5\text{ }\Omega\cdot\text{cm}$ ). In conventional processes variations up to 5% are normal on different wafers or different locations on the same wafer. Besides affecting  $Q$ , this would shift  $f_{SR}$ , in particular, on medium-resistivity substrates [24]. Nevertheless, the overall agreement between simulated and experimental  $L$ 's and  $Q$ 's on both substrates is good, bearing in mind that no fitting parameters were used.

A common shortcoming of many commercial, 2-D and two-and-one-half-dimensional (2.5-D) EM solvers is their inability to handle the finite thickness of the conductors: the metal layers are assumed to be infinitely thin, while the nonuniform current distribution in the vertical direction is accounted for by using an effective complex frequency-dependent sheet resistivity. The concentric-ring model, however, is not restricted to this planar approximation. In order to test the accuracy of the model in handling thick conductors, we built additional spiral inductors on the  $5\text{-}\Omega\cdot\text{cm}$  substrate with the thickness of the top metal layer ranging from 2 to  $4\text{ }\mu\text{m}$ . The quality factor of the 2-nH inductor built using a 1-, 2-, and  $4\text{-}\mu\text{m}$ -thick layer is shown in Fig. 10. Again, a good match is found between the simulated and measured data, although the model predicts a slightly higher  $Q$  at frequencies above 6 GHz as the metal thickness is increased.

#### IV. CONCLUSIONS

We have presented a semianalytical model for circular spiral inductors on layered substrates. The model employs the concen-

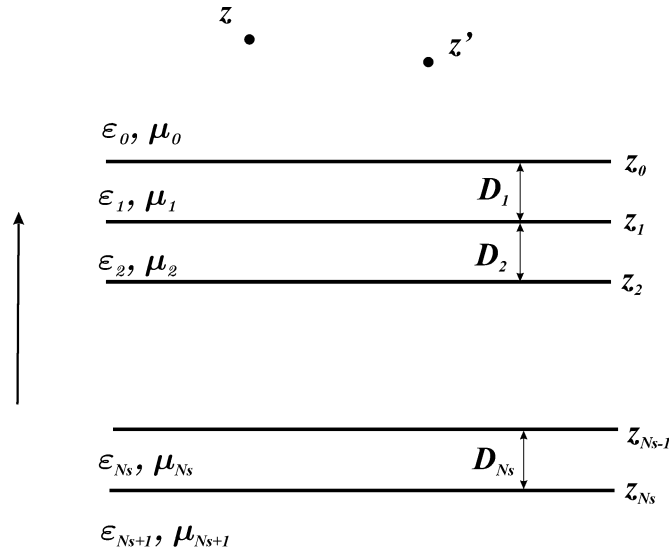


Fig. 11. Multilayered substrate used for the evaluation of the spectral-domain Green's functions.

tric-ring approximation where the circular inductor is replaced by the series connection of concentric rings. Using the rotational symmetry of the system of rings, as well as the quasi-1-D approximation, a semianalytical solution is derived for the MPIEs based on the Fourier series expansion of the potentials and currents in the rings. The results are in good agreement with experimental data for inductors of various sizes and metal thicknesses built on a lossy Si substrate.

#### APPENDIX

In order to calculate the functions  $\mathcal{K}^m$  and  $\mathcal{G}^m$  and their matrix elements, we start with the spectral representation of the Green's functions  $K$  and  $G$

$$G(R; z, z') = \int_0^\infty \tilde{G}(q|z, z') J_0(qR) \frac{q dq}{2\pi} \quad (31a)$$

$$K(R; z, z') = \int_0^\infty \tilde{K}(q|z, z') J_0(qR) \frac{q dq}{2\pi} \quad (31b)$$

where  $J_m$  denotes the  $m$ th-order Bessel function of the first kind and  $\tilde{G}$  and  $\tilde{K}$  are spectral-domain Green's functions.

Although the expressions for the spectral-domain Green's functions in stratified media can be found in various papers, we present them below for the sake of completeness. We restrict ourselves to the typical configuration of Fig. 11 where  $z$  and  $z'$  are both located above the substrate. (Although relevant, the more general, but complicated case where  $z$  and  $z'$  lie in arbitrary substrate layers will not be discussed here.) The functions  $\tilde{K}(q|z, z')$  and  $\tilde{G}(q|z, z')$  are then given by

$$\tilde{K}(q|z, z') = \frac{\mu_0}{2k_0} \left[ e^{-k_0|z-z'|} - \Gamma_0^T e^{-k_0(z+z'-2z_0)} \right] \quad (32a)$$

$$\begin{aligned} \tilde{G}(q|z, z') &= \frac{1}{2\epsilon_0 k_0} \left[ e^{-k_0|z-z'|} - \Gamma_0^L e^{-k_0(z+z'-2z_0)} \right] \\ &+ \frac{\mu_0 \omega^2}{2q^2 k_0} \left( \Gamma_0^L - \Gamma_0^T \right) e^{-k_0(z+z'-2z_0)} \end{aligned} \quad (32b)$$

where  $\Gamma_0^L$  and  $\Gamma_0^T$  are substrate reflection coefficients determined by the recursive relations

$$\Gamma_{p-1}^L = \frac{\Gamma_p^L + \xi_{p-1}^L e^{2k_p D_p}}{\Gamma_p^L \xi_{p-1}^L + e^{2k_p D_p}} \quad (33a)$$

$$\Gamma_{p-1}^T = \frac{-\Gamma_p^T + \xi_{p-1}^T e^{2k_p D_p}}{\Gamma_p^T \xi_{p-1}^T - e^{2k_p D_p}} \quad (33b)$$

$$\xi_{p-1}^L = \frac{\epsilon_p k_{p-1} - \epsilon_{p-1} k_p}{\epsilon_p k_{p-1} + \epsilon_{p-1} k_p} \quad (33c)$$

$$\xi_{p-1}^T = \frac{\mu_p k_{p-1} - \mu_{p-1} k_p}{\mu_p k_{p-1} + \mu_{p-1} k_p} \quad (33d)$$

$$\Gamma_{Ns}^L = \Gamma_{Ns}^T = 0 \quad (33e)$$

$$\begin{aligned} \epsilon_p &= \epsilon_p - j \frac{\sigma_p}{\omega} \\ k_p^2 &= q^2 - \mu_p \epsilon_p \omega^2 \end{aligned} \quad (33f)$$

where  $Ns$  is the number of substrate layers (the infinite layer beneath the substrate is denoted by  $Ns + 1$ ), and  $\epsilon_p$ ,  $\mu_p$ , and  $\sigma_p$  ( $p = 0, 1, \dots, Ns + 1$ ) are the dielectric constant, permeability, and conductivity of each layer, respectively (Fig. 11). The layer thicknesses are denoted by  $D_p$ .

From (11), (12c), (12d), (31a), (31b), and Neumann's addition theorem for Bessel functions [25]

$$J_0(qR) = \sum_{m=-\infty}^{\infty} J_m(qr) J_m(qr') \cos(m\varphi) \quad (34)$$

with  $\varphi = \theta - \theta'$ , it follows that

$$\begin{aligned} \mathcal{G}^m(r, z; r', z') &= \int_0^\infty \tilde{G}(q|z, z') J_m(qr) J_m(qr') q dq \end{aligned} \quad (35a)$$

$$\begin{aligned} \mathcal{K}^m(r, z; r', z') &= \int_0^\infty \tilde{K}(q|z, z') \left[ J_{m+1}(qr) J_{m+1}(qr') \right. \\ &\quad \left. + J_{m-1}(qr) J_{m-1}(qr') \right] \frac{q dq}{2}. \end{aligned} \quad (35b)$$

The matrices  $\check{\mathcal{G}}_{i\alpha, k\beta}^m$  and  $\check{\mathcal{K}}_{i\alpha, k\beta}^m$  are evaluated by substituting the above relationship into (20b) and (20c) and carrying out the integrations using the basis functions (21). Due to the exponential dependence of the spectral-domain Greens functions on  $z$  and  $z'$ , the integrations over those variables can be performed analytically, whereas those involving  $r$  are calculated by means of the relationships

$$\begin{aligned} \int_0^z J_{2m}(t) dt &= \int_0^z J_0(t) dt - 2 \sum_{h=0}^{m-1} J_{2h+1}(z) \\ \int_0^z J_{2m+1}(t) dt &= 1 - J_0(z) - 2 \sum_{h=1}^m J_{2h}(z) \\ \int_0^z J_0(t) dt &= z J_0(z) + \frac{\pi x}{2} [\mathbf{H}_0(z) J_1(z) - \mathbf{H}_1(z) J_0(z)] \end{aligned} \quad (36)$$

where  $\mathbf{H}_0$  and  $\mathbf{H}_1$  are Sturve functions. As a result, computation of each matrix element only requires the evaluation of a single integral over the variable  $q$ .

#### ACKNOWLEDGMENT

The author would like to thank J. N. Burghartz, H. Schellevis, and A. Akhnoikh, all of the Delft Institute of Microelectronics and Submicron Technology (DIMES), Delft, The Netherlands, for their support.

#### REFERENCES

- [1] A. E. Ruehli, "Inductance calculations in a complex integrated circuit environment," *IBM J. Res. Develop.*, vol. 16, pp. 470–481, 1972.
- [2] H. M. Greenhouse, "Design of planar rectangular microelectronic inductors," *IEEE Trans. Parts, Hybrids, Packag.*, vol. 10, pp. 101–109, 1974.
- [3] R. L. Remke and G. A. Burdick, "Spiral inductors for hybrid and microwave application," in *IEEE Proc. 24th Electronic Computation Conf.*, 1974, pp. 152–161.
- [4] P. A. Brennan, N. Raver, and A. E. Ruehli, "Three-dimensional inductance computations with partial element equivalent circuits," *IBM J. Res. Develop.*, vol. 23, pp. 661–667, 1979.
- [5] E. Pettepaul and H. Kapusta, "CAD models of lumped elements on GaAs up to 18 GHz," *IEEE Trans. Microwave Theory Tech.*, vol. 36, pp. 294–304, Feb. 1988.
- [6] A. C. Cangellaris, J. L. Prince, and L. P. Vakanas, "Frequency-dependent inductance and resistance calculation for three-dimensional structures in high-speed interconnect systems," *IEEE Trans. Comp., Hybrids, Manufact. Technol.*, vol. 13, pp. 154–159, Mar. 1990.
- [7] N. M. Nguyen and R. G. Meyer, "Si IC-compatible inductors and LC passive filters," *IEEE J. Solid-State Circuits*, vol. 25, pp. 1028–1031, Aug. 1990.
- [8] R. G. Arnold and D. J. Pedder, "Microwave characterization of microstrip lines and spiral inductors in MCM-D technology," *IEEE Trans. Comp., Hybrids, Manufact. Technol.*, vol. 15, pp. 1038–1045, Dec. 1992.
- [9] R. B. Merril, T. W. Lee, H. You, R. Rasmussen, and L. A. Moberly, "Optimization of high  $Q$  integrated inductors for multi-level metal CMOS," in *Proc. Int. Electron Devices Meeting Tech. Dig.*, 1995, pp. 983–986.
- [10] J. N. Burghartz, M. Soyuer, and K. A. Jenkins, "Microwave inductors and capacitors in standard multilevel interconnect silicon technology," *IEEE Trans. Microwave Theory Tech.*, vol. 44, pp. 100–104, Jan. 1996.
- [11] C. P. Yue, J. Lau, T. H. Lee, and S. S. Wong, "A physical model for planar spiral inductors on silicon," in *Proc. Int. Electron Devices Meeting Tech. Dig.*, 1996, pp. 155–158.
- [12] D. Lovelace, N. Camilleri, and G. Kannell, "Silicon MMIC inductor modeling for high volume, low cost applications," *Microwave J.*, pp. 60–71, Aug. 1994.
- [13] S. H. Song, H. B. Lee, H. K. Jung, S. Y. Hahn, K. S. Lee, C. Cheon, and H. S. Kim, "Spectral domain analysis of the spiral inductor on multilayer substrates," *IEEE Trans. Magn.*, vol. 33, pp. 1488–1491, Mar. 1997.

- [14] J. R. Mosig and F. E. Gardiol, "A dynamic radiation model for microstrip structures," in *Advances in Electronics and Electron Physics*, P. W. Hawkes, Ed. New York: Academic, 1982, vol. 59, pp. 139–237.
- [15] —, "General integral equation formulation for microstrip antennas and scatterers," *Proc. Inst. Elect. Eng.*, vol. 132, pp. 424–432, 1985.
- [16] K. A. Michalski and D. Zheng, "Electromagnetic scattering and radiation by surfaces of arbitrary shape in layered media. II. Theory," *IEEE Trans. Antennas Propagat.*, vol. 38, pp. 335–344, Mar. 1990.
- [17] M. Kahrizi, T. K. Sarkar, and Z. A. Maricevic, "Space domain approach for the analysis of printed circuits," *IEEE Trans. Microwave Theory Tech.*, vol. 42, pp. 450–457, Mar. 1994.
- [18] R. Bungler and F. Arndt, "Efficient MPIE approach for the analysis of three-dimensional microstrip structures in layered media," *IEEE Trans. Microwave Theory Tech.*, vol. 45, pp. 1141–1153, Aug. 1997.
- [19] T. Huan-Shang, L. J. Lin, R. C. Frye, K. L. Tai, M. Y. Lau, D. Kossives, F. Hrycenko, and C. Young-Kai, "Investigation of current crowding effects on spiral inductors," in *IEEE MTT-S Int. Microwave Symp. Dig.*, 1997, pp. 139–142.
- [20] A. M. Niknejad and R. G. Meyer, "Analysis, design, and optimization of spiral inductors and transformers for Si RF ICs," *IEEE J. Solid-State Circuits*, vol. 33, pp. 1470–1481, Oct. 1998.
- [21] —, "Analysis of eddy-current losses over conductive substrates with applications to monolithic inductors and transformers," *IEEE Trans. Microwave Theory Tech.*, vol. 49, pp. 166–176, Jan. 2001.
- [22] B. Rejaei, J. L. Tauritz, and P. Snoeij, "A predictive model for Si-based circular spiral inductors," in *IEEE MTT-S Int. Microwave Symp. Dig.*, 1998, pp. 148–154.
- [23] S. F. Mahmoud and E. Beyne, "Inductance and quality-factor evaluation of planar lumped inductors in a multilayer configuration," *IEEE Trans. Microwave Theory Tech.*, vol. 45, pp. 918–923, June 1997.
- [24] J. N. Burghartz and B. Rejaei, "On the design of RF spiral inductors on silicon," *IEEE Trans. Electron Devices*, vol. 50, pp. 718–729, Mar. 2003.
- [25] M. Abramowitz and I. A. Stegun, *Handbook of Mathematical Functions With Formulas, Graphs, and Mathematical Tables*. New York: Wiley, 1972.



**Behzad Rejaei** received the M.Sc. degree in electrical engineering from the Delft University of Technology, Delft, The Netherlands, in 1990, and the Ph.D. degree in theoretical condensed matter physics from the University of Leiden, Leiden, The Netherlands, in 1994.

From 1995 to 1997, he was a member of the physics faculty with the Delft University of Technology, where he performed research on mesoscopic charge–density–wave systems. Since 1997, he has been with the Department of Electrical Engineering, Mathematics, and Computer Science, Delft University of Technology, where he is currently an Associate Professor. His research interests are in the areas of EM modeling of integrated passive components and physics of ferromagnetic devices.